1 **Aggravated surface O₃ pollution primarily driven by meteorological variation**

2 **in China during the early COVID-19 pandemic lockdown period**

4 Zhendong Lu[1*], Jun Wang[1,2*], Yi Wang[2,3], Daven K. Henze[4], Xi Chen[2], Tong Sha[2,5], Kang Sun[6,7]

6 [1]*Interdisciplinary Graduate Program in Informatics, The University of Iowa, Iowa City, IA,*

7 *United States*

8 [2]*Department of Chemical and Biochemical Engineering, Center for Global and Regional*

9 *Environmental Research and Iowa Technology Institute, The University of Iowa, Iowa City, IA,*

10 *United States*

11 [3]*Now at Hubei Key Laboratory of Regional Ecology and Environmental Change, School of*

12 *Geography and Information Engineering, China University of Geosciences, Wuhan, China*

13 [4]*Department of Mechanical Engineering, University of Colorado, Boulder, CO, United States*

14 [5]*Now at Collaborative Innovation Center on Forecast and Evaluation of Meteorological*

15 *Disasters (CIC-FEMD), Key Laboratory for Aerosol-Cloud-Precipitation of China*

16 *Meteorological Administration, Nanjing University of Information Science and Technology,*

17 *Nanjing, China*

18 [6]*Department of Civil, Structural and Environmental Engineering, University at Buffalo, Buffalo,*

19 *NY, United States*

20 [7]*Research and Education in Energy, Environment and Water Institute, University at Buffalo,*

21 *Buffalo, NY, United States*

23 *Correspondence to: Jun Wang (jun-wang-1@uiowa.edu) and Zhendong Lu (zhendong-

24 lu@uiowa.edu)

26   November 2023

Abstract

Due to the lockdown during the COVID-19 pandemic in China from late January to early April in 2020, a significant reduction of primary air pollutants has been identified by satellite and ground observations. However, this reduction is in contrast with the increase of surface O_3 concentration in many parts of China during the same period. The reasons for this contrast are studied here from two perspectives: emission changes and inter-annual meteorological variations. Based on top-down constraints of NOx emissions from TROPOMI measurements and GEOS-Chem model simulations, our analysis reveals that NOx and volatile organic compound (VOC) emission reductions as well as meteorological variations lead to 8%, -3%, and 1% changes in O_3 over North China, respectively. In South China, however, we find that meteorological variations cause ~30% increases in O_3, which is much larger than -1% and 2% changes due to VOC and NOx emission reductions, respectively, and the overall O_3 increase is consistent with the surface observations. The higher temperature is the main reason that leads to the surface O_3 increase in South China. Overall, inter-annual meteorological variations have a larger impact than emission reductions on the aggravated surface O_3 pollution in China during the early lockdown period of COVID-19 pandemic.

1. Introduction

Surface ozone (O_3), an important air pollutant that is harmful to human health (Jerrett et al., 2009) and stomatal conductance of green vegetations (Gong et al., 2020), is produced by photochemical reactions of nitrogen oxides (NOx) and volatile organic compounds (VOC) (Liu et al., 1987; Sillman et al., 1990). In addition to emissions, meteorological conditions, such as temperature, solar radiation and relative humidity, also have large impacts on surface O_3 formation (Lu et al., 2019).

Ground observations show that surface O_3 increased dramatically during the COVID-19 lockdown period in China by around 40% on average (Tong et al., 2023) and even larger than 100% (Shi and Brasseur, 2020; Liu et al., 2021) depending on the time period and region. The reduction of economic activities during the lockdown period led to a significant decrease of several primary air pollutants emissions. The NO_2 vertical column density (VCD) from satellite measurements and surface NO_2 concentration from ground measurements were reduced by 40% - 60% in China during the lockdown period (Bauwens et al., 2020; Shi and Brasseur, 2020; Liu et al., 2020a; Zhang

59   et al., 2020). A lower but discernible reduction of sulfur dioxide (SO_2), carbon monoxide (CO),

60   and formaldehyde (HCHO) have also been identified by satellite or ground-based observations in

61   China (Shi and Brasseur, 2020; Levelt et al., 2022; Ghahremanloo et al., 2021). However, during

62   this period surface O_3 concentrations increased, and the respective roles of meteorological factor

63   and emission reduction for the aggravated surface O_3 pollution during the lockdown in China need

64   to be further quantified.

65   This study provides a quantitative analysis of the causes for the unexpectedly aggravated

66   surface O_3 pollution in China during the early lockdown period of the pandemic from two

67   perspectives using GEOS-Chem model. One is anthropogenic emission reduction of NOx and

68   VOC in response to the lockdown possibly under a VOC-limiting chemical regime of surface O_3

69   production (Guo et al., 2023), while the other is the impact of natural variability of meteorological

70   conditions. Previous studies have reported the enhanced surface O_3 due to NOx emission decline

71   during the lockdown period in North China using chemical transport model (CTM) simulations

72   without controlling for the impacts of meteorological variability (Zhang et al., 2021; Huang et al.,

73   2020; Miyazaki et al., 2020). Other studies quantified or excluded the meteorological impacts on

74   the surface O_3 using statistical analysis instead of CTM that account for the physical and chemical

75   processes (Venter et al., 2020; Bi et al., 2022; Tong et al., 2023). Although a few studies have

76   investigated the contributions from both emission reduction and meteorological variability to

77   surface O_3 increase using CTMs, most of their results have uncertainties due to the limitations of

78   their analysis. For example, some of them keep the emissions unchanged (Zhao et al., 2020) or

79   assume an arbitrarily uniform emission reduction instead of constraining the emission based on

80   observations (Le et al., 2020; Liu et al., 2021). In cases where the emissions were constrained by

81   the observations, the focus was limited to several cities in China (Liu et al., 2020b). Furthermore,

82   in the past studies, the surface O_3 increase during the lockdown period of 2-4 weeks is quantified

83   in reference to the time period right before the lockdown instead of the same period in previous

84   years; such comparisons by design cannot exclude the possibility that the seasonal variation of

85   meteorology from early January to early April may have dominated the cause for the surface O_3

86   increase. A comprehensive analysis of the contributions from emission reductions and

87   meteorological variations to the surface O_3 increase during the first round of the lockdown period

88   with respect to the same time period in previous years in China is therefore overdue.

89   Here, we apply a top-down method to update NOx and VOC emission in February and
90   March in 2020 based on the TROPOMI NO$_2$ and formaldehyde (HCHO) product. A set of GEOS-
91   Chem model simulations with NOx and VOC emissions and meteorological fields in different time
92   periods are then conducted. Based on the difference in surface O$_3$ concentration in different
93   modeling sensitivity experiments, we quantitatively assess the respective roles of emission and
94   meteorology in regulating surface O$_3$ concentration in continental China. The ground observations
95   of surface O$_3$ and NO$_2$ concentration are compared with the model simulations to verify our
96   analysis. Section 2 introduces the satellite and ground-based measurements, NOx emission update
97   scheme, and the configurations of GEOS-Chem simulation experiments. Section 3 provides an
98   evaluation of the constrained NOx emission and surface O$_3$ simulations. The analysis of the
99   mechanism of the aggravated surface O$_3$ pollution is presented in Section 4, followed by the
100   summary and conclusions in Section 5.

101

102   **2. Datasets and Methods**

103   **2.1 TROPOMI NO$_2$ and HCHO product**

104   We used tropospheric NO$_2$ and HCHO level 2 VCD product provided by the Tropospheric
105   Monitoring Instrument (TROPOMI) onboard the Sentinel-5 Precursor (S5P) satellite (Veefkind et
106   al., 2012). S5P is a sun-synchronous polar orbit satellite launched on 13 October 2017, which
107   covers the near-global domain in a single day. TROPOMI provides NO$_2$ and HCHO retrievals at
108   an approximately 7 km x 3.5 km spatial resolution (5.5km x 3.5 km since 6 August 2019) from the
109   ascending orbit with an equatorial crossing time of ~13:30 local time (Van Geffen et al., 2020; De
110   Smedt et al., 2018). The datasets were obtained from the NASA Goddard Earth Sciences Data and
111   Information Services Center (https://daac.gsfc.nasa.gov). A quality control procedure similar to
112   Bauwens et al. (2020) but with slightly stricter criteria is adopted for TROPOMI NO$_2$ and HCHO
113   data. The TROPOMI retrievals under one or more than one of the following conditions are
114   screened out for data quality control. (1) Quality assurance value is no larger than 0.5; (2) cloud
115   radiance fraction within NO$_2$ or HCHO retrieval window is larger than 0.3; (3) solar zenith angle
116   is larger than 70°; and (4) viewing zenith angle is larger than 70°.

117

118   **2.2 Ground O$_3$ and NO$_2$ measurements**

119   Surface measurements of O_3 and NO_2 were collected from ~1600 operational air quality

120   monitoring stations over the mainland China managed by the China National Environmental

121   Monitoring Center (http://www.cnemc.cn/en/). We calculated daily maximum 8-hour average

122   (MDA8) O_3 concentration from hourly in situ measurements. Surface O_3 are measured by

123   ultraviolet photometric method and Indigo disulfonate spectrophotometry, following the national

124   environmental standards of HJ 590-2010 and HJ 504-2009. Surface NO_2 concentrations are

125   measured by the chemiluminescence method (Zhang and Cao, 2015), which can cause a positive

126   bias in the NO_2 measurements (Steinbacher et al., 2007). The true NO_2 concentrations only account

127   for 43%-76% and 70%-83% of measured values for rural and urban sites (Steinbacher et al., 2007).

128   Following Wang et al. (2020b), we also applied a correction factor but with a lower value of 0.75

129   to the measured NO_2, considering that we included both rural and urban sites. The sampling ports

130   are placed at 3 to 15 meters above the ground following the national environmental monitoring

131   method standard HJ 664-2013. The measured data are reported in the unit of µg m^{-3} under standard

132   temperature (273.15 K) and pressure (101.325 kPa) according to national environmental standards

133   GB 3095-2012.

134

135   **2.3 GEOS-Chem model and its adjoint**

136   The global 3-D chemical transport model GEOS-Chem (Bey et al., 2001) version 12.7.2 is

137   used here. We apply the nested-grid version of GEOS-Chem (Chen et al., 2009; Wang et al., 2004)

138   with the horizontal resolution of 0.25°×0.3125° and 47 vertical hybrid-sigma levels over East Asia

139   (70°E-140°E, 15°N-55°N). The boundary conditions are obtained from the 2°×2.5° global

140   simulation. The model is driven by the GEOS-FP meteorological field provided by NASA Global

141   Modeling and Assimilation Office (GMAO). A detailed O_3-NOx-hydrocarbon chemistry (Mao et

142   al., 2010; Mao et al., 2013; Travis et al., 2016) is included in the GEOS-Chem model. The altitude

143   of the surface O_3 output from GEOS-Chem is specified at 9 meters above the ground to match the

144   in-situ measurements (Travis et al., 2017; Zhang et al., 2012). Through our sensitivity test using

145   GEOS-Chem, the variation of surface O_3 from 3 to 9 meters above the surface is generally less

146   than 0.723 ppb (75th percentile), and the median bias is 0.283 ppb. Travis et al. (2017) reported

147   from 60 m to 10 m above the ground, the MDA8 O_3 could decrease by ~3 ppb. Therefore, when

148   comparing GEOS-Chem surface O3 with in-situ measurements, the differences caused by

149   inconsistent reported altitudes (9 m versus 3-15 m) can be ignored.

150   The global anthropogenic emission used in GEOS-Chem model is the Community

151   Emissions Data System (CEDS) inventory (Hoesly et al., 2018), which is replaced by the MIX

152   inventory (Li et al., 2017) over the Asian region. Biogenic emissions for VOCs follows the Model

153   of Emissions of Gases and Aerosols from Nature (MEGAN) inventory (Guenther et al., 2012).

154   Natural NOx emissions includes biomass burning from GFED4 inventory (Van Der Werf et al.,

155   2017), soil NOx emissions (Hudman et al., 2012) and lightning sources (Murray et al., 2012; Ott

156   et al., 2010).

157   The adjoint of the GEOS-Chem model (Henze et al., 2007; Henze et al., 2009) is a

158   component of the 4D-Var inversion method that can efficiently optimize spatially disaggregated

159   aerosol and gas emissions. This is done through iterative minimization of a cost function using the

160   model adjoint to calculate the gradient of the cost function with respect to a large number of model

161   parameters (such as anthropogenic NOx emissions in each grid box) simultaneously. The cost

162   function is the sum of the error weighted difference between forward model outputs and

163   observations and the divergence of posterior model parameters from the prior estimate (Section

164   2.4). We developed and validated the observation operator for TROPOMI NO$_2$ in the GEOS-Chem

165   adjoint model version 35n similar to Wang et al. (2020a) and used it to optimize the anthropogenic

166   NOx emission during the lockdown period in China. The NOx emission optimization is

167   implemented using the 4D-Var method with GEOS-Chem adjoint at the nested grid with the

168   resolution of 0.25°×0.3125°. The prior anthropogenic NOx emission used in the GEOS-Chem

169   adjoint is HTAP version 2 (Janssens-Maenhout et al., 2015), which is equivalent to the MIX

170   inventory in East Asia (Li et al., 2017).

171

172   **2.4 NOx and VOC emission updates**

173   Two approaches are used to update the emissions during the lockdown period in 2020. The

174   first is a simple mass balance approach (Leue et al., 2001; Martin et al., 2003; Vinken et al., 2014)

175   for updating the NOx emission by assuming a constant NOx lifetime and NOx/NO$_2$ ratio. In the

176   period from 2010 to 2019, the anthropogenic NOx emissions have declined significantly as a result

177   of the clean air actions of Chinese government (Zheng et al., 2018). We scale the anthropogenic

178   NOx emission from year 2010 to 2019 using the spatially gridded ratio of mean TROPOMI

179   tropospheric NO$_2$ VCD in Feb.-Mar. 2019 to GEOS-Chem simulated NO$_2$ column with default

180   MIX 2010 emission (Appendix A), to obtain the baseline anthropogenic NOx emission in 2019,

181   which is denoted as MIX 2019. To derive anthropogenic NOx emissions in 2020 in China during

182   the COVID-19 lockdown (MIX 2020), the spatially gridded ratio of mean TROPOMI tropospheric

183   NO₂ VCD in 2020 Feb.-Mar. to that in 2019 Feb.-Mar. is taken as a scaling factor for the updated

184   baseline anthropogenic NOx emission in 2019 (MIX 2019). The two-month mean of TROPOMI

185   NO₂ VCD in 2019 and 2020 are calculated with the physical oversampling procedure (Sun et al.,

186   2018). Scaling factors in regions where mean TROPOMI tropospheric NO₂ VCD in 2019 Feb.-

187   Mar. is less than 0.1 Dobson unit (DU) are set to 1 for emission updates in both 2020 and 2019,

188   assuming that the lockdown only affects the populated areas (that have high NO₂ in 2019).

189   The second method for updating NOx emission is 4D-Var via the GEOS-Chem adjoint

190   model. The anthropogenic NOx emissions in 2020 lockdown period derived from the GEOS-Chem

191   adjoint is denoted as 2020 Adjoint. Following Wang et al. (2020a), the cost function J for

192   optimizing the NOx emission is defined as

$$J = \frac{1}{2}\sum_{c\in\Omega}[H(\boldsymbol{c}) - \boldsymbol{s}]^{\mathrm{T}}\boldsymbol{S}_{\mathrm{obs}}^{-1}[H(\boldsymbol{c}) - \boldsymbol{s}] + \frac{1}{2}\gamma(\boldsymbol{\sigma} - \boldsymbol{\sigma}_a)^{\mathrm{T}}\boldsymbol{S}_a^{-1}(\boldsymbol{\sigma} - \boldsymbol{\sigma}_a) \tag{1}$$

194   where $\boldsymbol{s}$ is the tropospheric slant column density of TROPOMI NO₂, which is the product of

195   TROPOMI NO₂ VCD and air mass factor. H is the TROPOMI NO₂ observation operator that maps

196   the modeled NO₂ concentrations $\boldsymbol{c}$ to the observations in time and space and calculates the

197   corresponding slant column density to make an apple-to-apple comparison of the model to

198   TROPOMI. Ω is the spatial and temporal domain where both model simulations and observations

199   are available. $\boldsymbol{\sigma}$ is the scaling factor of anthropogenic NOx emissions to be optimized, and $\boldsymbol{\sigma}_a$ is

200   the prior emission scaling factors, which equals 1. $\boldsymbol{S}_{\mathrm{obs}}$ and $\boldsymbol{S}_a$ are observational and prior error

201   covariance matrices, respectively. γ is the regularization factor that balances the weights of the

202   observational term and prior term. We assumed $\boldsymbol{S}_{\mathrm{obs}}$ to be diagonal following Wang et al. (2020a)

203   with the diagonal values calculated as the square of the standard error of tropospheric NO₂ slant

204   column density from the TROPOMI product. The prior error of the NOx emissions is assumed to

205   be 100%. The spatial correlation of NOx emissions is considered in this study, and the off-diagonal

206   elements of $\boldsymbol{S}_a$ are computed by assuming an exponentially decaying error correlation with a fixed

207   decaying distance of 150 km following Qu et al. (2017). The γ value was determined as 500 via

208   the total error minimization and L-curve test (Henze et al., 2009; Qu et al., 2017).

209   We developed the observation operator for TROPOMI NO₂ product in the GEOS-Chem

210   adjoint model with GEOS-Chem NO₂ vertical profiles and TROPOMI NO₂ averaging kernel

211   applied to minimize the discrepancies between the assumptions in TROPOMI NO_2 retrieval and

212   GEOS-Chem model simulation. See Appendix B for additional details. The observation operator

213   has been validated using the finite difference method (Appendix C).

214   For anthropogenic VOC emissions update, we only applied the mass balance method based

215   on the TROPOMI HCHO data. The default anthropogenic VOC emissions used in the GEOS-

216   Chem is also MIX 2010 (Li et al., 2017). We ignore the change of anthropogenic VOC emissions

217   from 2010 to 2019. The baseline VOC emission in 2019 (MIX 2019) is identical to that of MIX

218   2010. The updated anthropogenic VOC emissions during the lockdown period is denoted as MIX

219   2020. HCHO is one species of VOC and may not be able to represent other VOC species. Different

220   from NOx, biogenic sources, meteorological impacts, and large retrieval uncertainty of HCHO due

221   to its low optical depth prevent accurately quantifying the emission decline due to lockdown from

222   satellite retrievals (Levelt et al., 2022). To optimize the signal, we spatially aggregate the ratio of

223   TROPOMI HCHO during the lockdown period to that before the lockdown to the resolution of

224   0.5°, which are used as the scaling factors for updating the anthropogenic VOC emissions during

225   the lockdown period. The aggregation is based on the oversampling of TROPOMI HCHO at 0.01°

226   resolution, and the ratio is computed as the mean of the lowest 25th percentile of all ratios at 0.01°

227   resolution in each 0.5°×0.5° grid box, which ensures that only statistically significant changes are

228   considered. We assumed the change of anthropogenic VOC emissions over sparsely populated

229   areas (TROPOMI NO_2 in 2019 Feb.-Mar. less than 0.1 DU) is insignificant and assigned the ratio

230   values as one. To further evaluate the uncertainties associated with this approach, we also

231   conducted sensitivity study by using different threshold in the aggregation.

232   We assess the results from model experiments (as described in Section 2.5) adopting the

233   updated NOx emission by comparing mean tropospheric NO_2 VCD from GEOS-Chem and from

234   TROPOMI observations in Feb.-Mar. of 2019 and 2020. The averaging kernel of TROPOMI NO_2

235   is applied to modeled NO_2 column for this comparison, following Sha et al. (2021). Further

236   quantitative evaluation of the model results also used the surface observation of O_3 and NO_2.

237

238   **2.5 GEOS-Chem model experiments**

239   A series of sensitivity experiments is conducted over China with different NOx and VOC

240   emissions and GEOS-FP meteorological fields in different years using GEOS-Chem (v12.7.2)

241   model. All simulations are conducted from Jan. 15 to Mar. 31. The 17 days before Feb. 1 are used

242   for spin up, and the model output for Feb. and Mar. are used for the analysis. The configurations

243   of different simulations are listed in Table 1.

244

245   **Table 1.** Configurations of model sensitivity experiments.

Experiments	Abbreviation	Meteorology	NOx Emission	VOC Emission
Baseline (2019)	2019B	GEOS-FP 2019	MIX 2019	MIX 2019
2020 Default	2020D	GEOS-FP 2020	MIX 2019	MIX 2019
2020 NOx	2020N	GEOS-FP 2020	MIX 2020	MIX 2019
2020 VOC	2020V	GEOS-FP 2020	MIX 2019	MIX 2020
2020 Lockdown	2020L	GEOS-FP 2020	MIX 2020	MIX 2020
2020 Adjoint	2020A	GEOS-FP 2020	Adjoint 2020	MIX 2020

246

247   We use the following equations to quantify the contributions from NOx and VOC emission

248   reduction due to COVID-19 and meteorological variation to the increase of surface O₃.

249
$$\Delta O_3^{\text{NOx}} = \frac{O_3^{2020A} - O_3^{2020V}}{O_3^{2019B}} \times 100\% \tag{2}$$

250
$$\Delta O_3^{\text{VOC}} = \frac{O_3^{2020L} - O_3^{2020N}}{O_3^{2019B}} \times 100\% \tag{3}$$

251
$$\Delta O_3^{\text{ems}} = \frac{O_3^{2020A} - O_3^{2020D}}{O_3^{2019B}} \times 100\% \tag{4}$$

252
$$\Delta O_3^{\text{met}} = \frac{O_3^{2020D} - O_3^{2019B}}{O_3^{2019B}} \times 100\% \tag{5}$$

253   Where ΔO_3^{NOx}, ΔO_3^{VOC} and ΔO_3^{ems} are the relative differences in surface O₃ concentration caused

254   by emission decline of NOx, VOC, and both NOx and VOC resulting from COVID-19. ΔO_3^{met}

255   represents the relative contribution to the surface O₃ change from the meteorological variation

256   between 2 years. O_3^{2019B}, O_3^{2020D}, O_3^{2020N}, O_3^{2020V}, O_3^{2020L} and O_3^{2020A} are mean MDA8 surface

257   O₃ concentration simulated by modeling experiments Baseline (2019), 2020 Default, 2020 NOx,

258   2020 VOC, 2020 Lockdown and 2020 Adjoint, respectively (Table 1).

259   The difference in simulated surface O₃ between 2020 and 2019, is the result of both

260   emission reductions and meteorological variations and is denoted as ΔO_3^{all}. It is calculated as

261   follows and is evaluated against the observed relative difference of mean MDA8 O_3 in Feb. to Mar.

262   between 2019 and 2020 at all ground sites:

263
$$\Delta O_3^{\text{all}} = \frac{O_3^{2020A} - O_3^{2019B}}{O_3^{2019B}} \times 100\% \qquad (6)$$

264

3. Results of model development, emissions, and validation

3.1 Changes of NOx and VOC emissions during COVID

267   We updated the anthropogenic NOx emissions during the COVID lockdown using both

268   4D-Var and mass balance methods (Fig. 1 and 2). The NOx emissions from the 4D-Var inversion

269   share a similar spatial pattern and magnitude with those found using the mass balance method (Fig.

270   1). However, the NOx emissions from the 4D-Var inversion are lower overall than those from the

271   mass balance method over North China by ~10% and larger over central China by ~40%. Fig. 2(a-

272   b) shows that the 4D-Var NOx emission reduction is more severe over urban regions and displays

273   a smoother spatial pattern than that from the mass balance approach, which is caused by the

274   arbitrary cut off with 0.1 DU of NO_2 VCD in the latter. Furthermore, the 4D-Var inversion

275   captured the NOx emission decline in Northeast China where the mass balance approach did not

276   because of the low NO_2 VCD. During Feb.-Mar. 2020, the anthropogenic NOx emissions in East

277   China decreased by ~30% compared to those in the same period in 2019. We also scale the

278   anthropogenic VOC emissions based on the TROPOMI HCHO data (Fig. 2(c)). The VOC

279   emissions decrease by ~20%-30% in East and South Asia. The anthropogenic VOC emission

280   changes in sparsely populated areas over Northwest China are neglected.
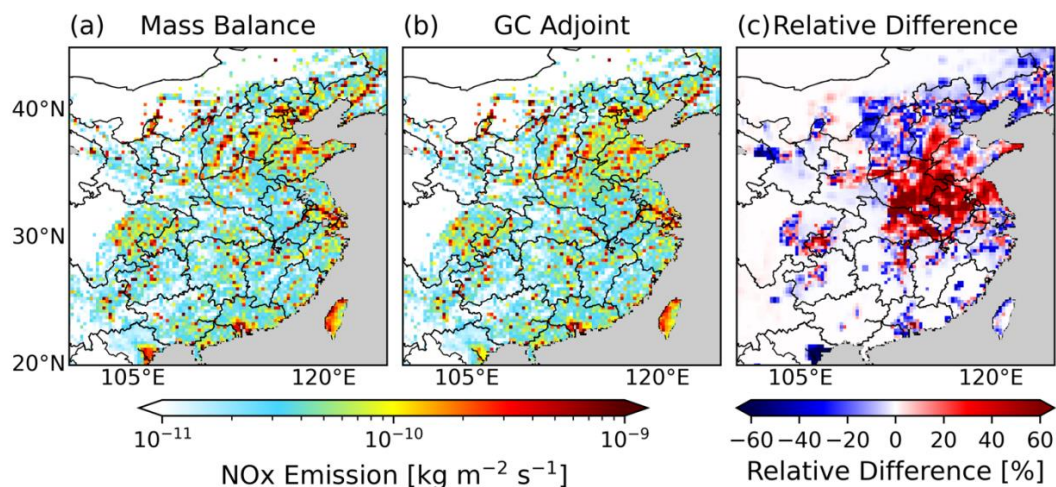
Figure 1. Updated anthropogenic NOx emission during Feb.-Mar. 2020 from (a) mass balance method, (b) 4D-Var method and (c) their relative difference.
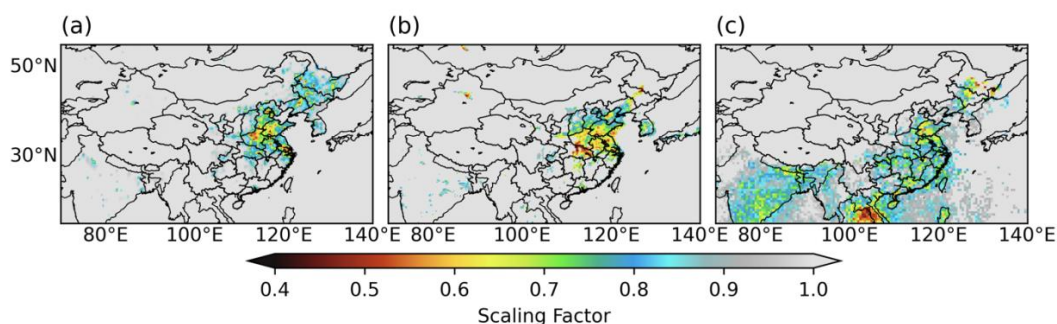
Figure 2. Scaling factors for anthropogenic NOx emission in Feb.-Mar. from 2019 to 2020 as derived from (a) 4D-Var, (b) mass balance. Scaling factors for anthropogenic VOC emissions from the mass balance are in (c).

3.2 Validation of NO$_2$ simulations

We further assess our updated anthropogenic NOx emissions by comparing the NO$_2$ VCD from TROPOMI with that from GEOS-Chem with the anthropogenic NOx emissions before and after the scaling (Fig. 3 and 4). Before updating the NOx emissions, the 2020 Default (Fig. 3(b)) simulation significantly overestimates the NO$_2$ VCD compared to the TROPOMI NO$_2$ observations (Fig. 3(a)). With the NOx emissions updated, the simulations 2020 NOx (Fig. 3(c))

296   and 2020 Adjoint (Fig. 3(d)) exhibit a much better agreement with TROPOMI NO$_2$ observation

297   than 2020 Default. However, Fig. 3(c) shows the GEOS-Chem simulation with the NOx emissions

298   from mass balance approach overestimated the NO$_2$ VCD over Beijing and southwest of Hebei

299   Province (pink and black circles in Fig.3) compared with TROPOMI data. The reason is that

300   scaling factors are applied only to anthropogenic NOx emissions, not total NOx emissions, so it is

301   expected that the model may still overestimate the NO$_2$ column after scaling part of the total NOx

302   emission. With the anthropogenic NOx emissions optimized by the 4D-Var method, the

303   overestimation of NO$_2$ VCD over Beijing and southwest of Hebei Province (pink and black circles

304   in Fig. 3) is mitigated compared with the NOx emissions from mass balance approach.

305   Fig. 4 further displays the statistics for the comparison between the TROPOMI NO$_2$ and

306   GEOS-Chem simulations via the scatterplot. The Baseline (2019) simulation captures the

307   magnitude of NO$_2$ VCD observations in 2019 well (Fig. 4(a)). The root-mean-square-error (RMSE)

308   and mean bias error (MBE) for the simulation with 2020 NOx emission derived from mass balance

309   method (Fig. 4(b)) decreased by 0.050 DU and 0.057 DU as compared to the 2020 Default (Fig.

310   4(c)). Compared with the result from GEOS-Chem simulation 2020 NOx, emissions from 2020

311   Adjoint (Fig. 4(d)) further led to the reduction of the MBE of the NO$_2$ VCD by 0.006 DU and

312   improve the correlation coefficient by 0.003. The significant overestimation of several pixels with

313   TROPOMI NO$_2$ VCD larger than 0.4 DU by the simulation 2020 NOx is also mitigated by 2020

314   Adjoint. The MBE between GEOS-Chem and TROPOMI for Baseline (2019), 2020 NOx and

315   2020 Adjoint are -0.004, 0.015 and 0.009 DU, respectively. The corresponding relative bias are

316   1.9%, 10% and 6.0%, which are all less than the relative uncertainty of ~30% for TROPOMI

317   tropospheric NO$_2$ VCD over East China (Van Geffen et al., 2022). The improved agreement

318   between the simulation with updated NOx emission and TROPOMI NO$_2$ provides a basis for

319   further analyzing the mechanism of aggravated surface O$_3$ pollution.

320
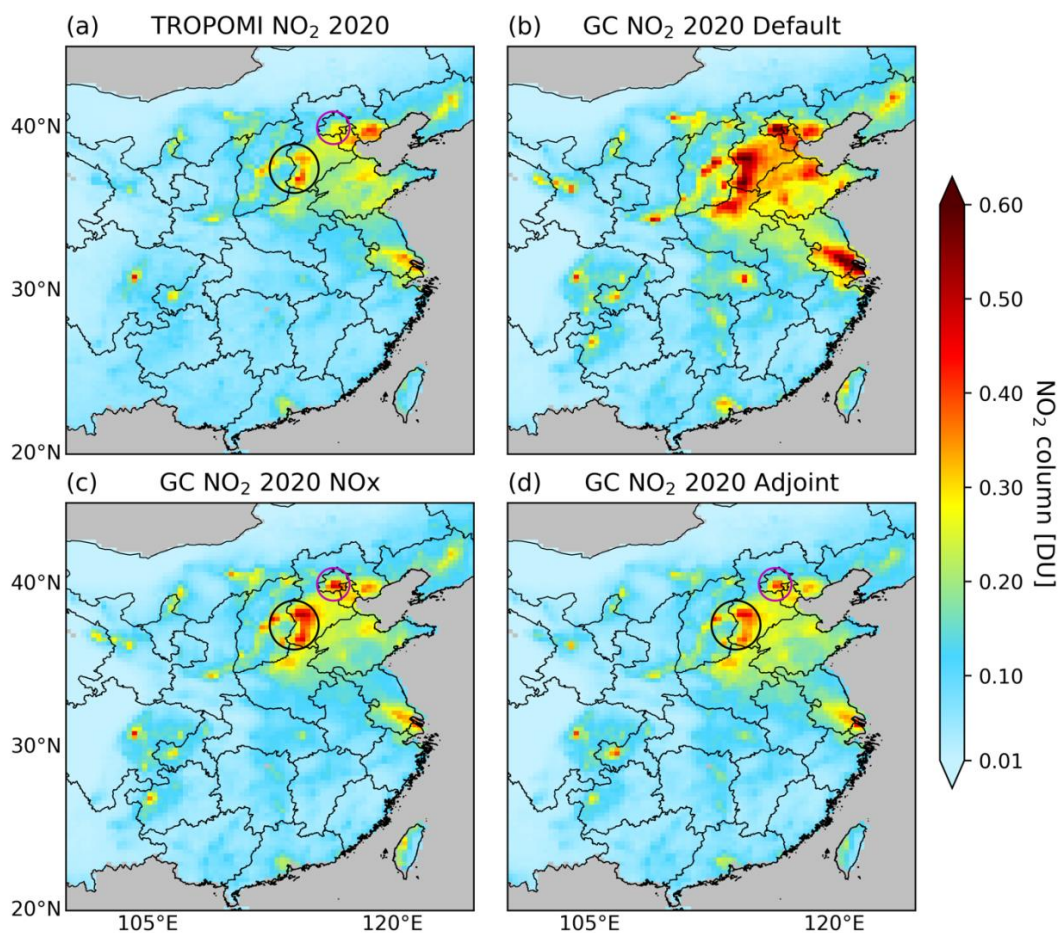
Figure 3. Comparison of tropospheric NO$_2$ VCD from (a) TROPOMI product in 2020 Feb.-Mar
with that from GEOS-Chem simulations (b) 2020 Default, (c) 2020 NOx and (d) 2020 Adjoint.
The pink and black circles mark the areas where NOx emissions from 4D-Var mitigated the NO$_2$
overestimation by mass balance method. The emissions and meteorology configurations for
GEOS-Chem simulations 2020 Default, 2020 NOx and 2020 Adjoint are listed in Table 1.

326
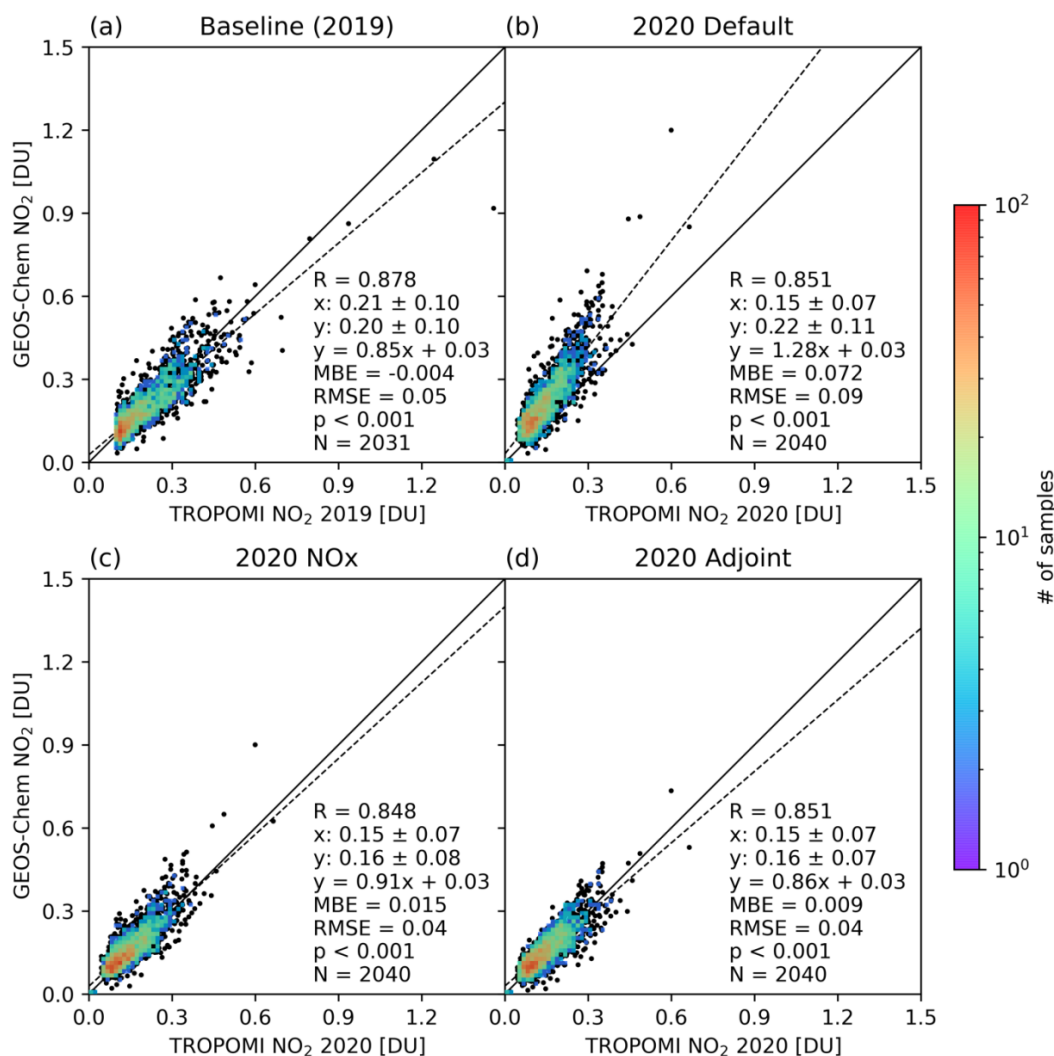
Figure 4. Scatter plot of TROPOMI NO₂ VCD versus the GEOS-Chem simulations for (a)
Baseline (2019), (b) 2020 Default, (c) 2020 NOx and (d) 2020 Adjoint, respectively. TROPOMI
data in Feb.-Mar. of 2019 was used in (a), and that of 2020 was used in (b-d). The emissions and
meteorology configurations for GEOS-Chem simulations are listed in Table 1. Only pixels with
TROPOMI NO₂ VCD in 2019 Feb.-Mar. larger than 0.1 DU are included in all comparisons.

335   Fig. 5 and Fig. 6 show the comparison of surface NO_2 between ground measurements and

336   GEOS-Chem simulations. The GEOS-Chem simulations Baseline (2019) (Fig. 5(b)) and 2020

337   Adjoint (Fig. 5(d)) both capture the spatial pattern and magnitude of surface NO_2 measurements

338   in Feb.-Mar. of 2019 (Fig. 5(a)) and 2020 (Fig. 5(c)) well, respectively. Fig. 6 further displays the

339   good agreements of surface NO_2 from Baseline (2019) (Fig. 6(a)) and 2020 Adjoint (Fig. 6(b)) to

340   the in-situ measurements via scatter plots. Table 2 displays the evaluation statistics, including the

341   correlation coefficient (R), MBE, RMSE and the slope and intercept of the linear regression, for

342   the simulated surface NO_2 from various simulation experiments compared with the in-situ

343   measurements. The correlation coefficient, MBE and RMSE between the simulation Baseline

344   (2019) and ground measurements in 2019 Feb.-Mar. are 0.724, 1.572 µg m^{-3} and 8.49 µg m^{-3},

345   respectively. Without updating the NOx emissions in 2020, the simulation 2020 Default

346   overestimate the ground measurements of surface NO_2 in 2020 Feb.-Mar (Table 2). The slope for

347   the linear regression is 1.19, and the MBE and RMSE are 6.021 µg m^{-3} and 10.43 µg m^{-3},

348   respectively (Table 2). After updating the NOx emissions, the GEOS-Chem simulations 2020 NOx

349   and 2020 Adjoint have good agreements with the in-situ measurements in 2020 Feb.-Mar. The

350   correlation coefficient between the simulation 2020 Adjoint versus the in-situ measurements is

351   0.651, higher than that of 0.608 for the simulation 2020 NOx versus the ground measurements

352   (Table 2). The MBE and RMSE of 2020 Adjoint (0.683 µg m^{-3} and 6.68 µg m^{-3}) are lower than

353   those of 2020 NOx (1.726 µg m^{-3} and 7.74 µg m^{-3}) (Table 2). This result further indicates the

354   superiority of 4D-Var for optimizing NOx emissions compared with the mass balance method

355   (Cooper et al., 2017; Streets et al., 2013).

356
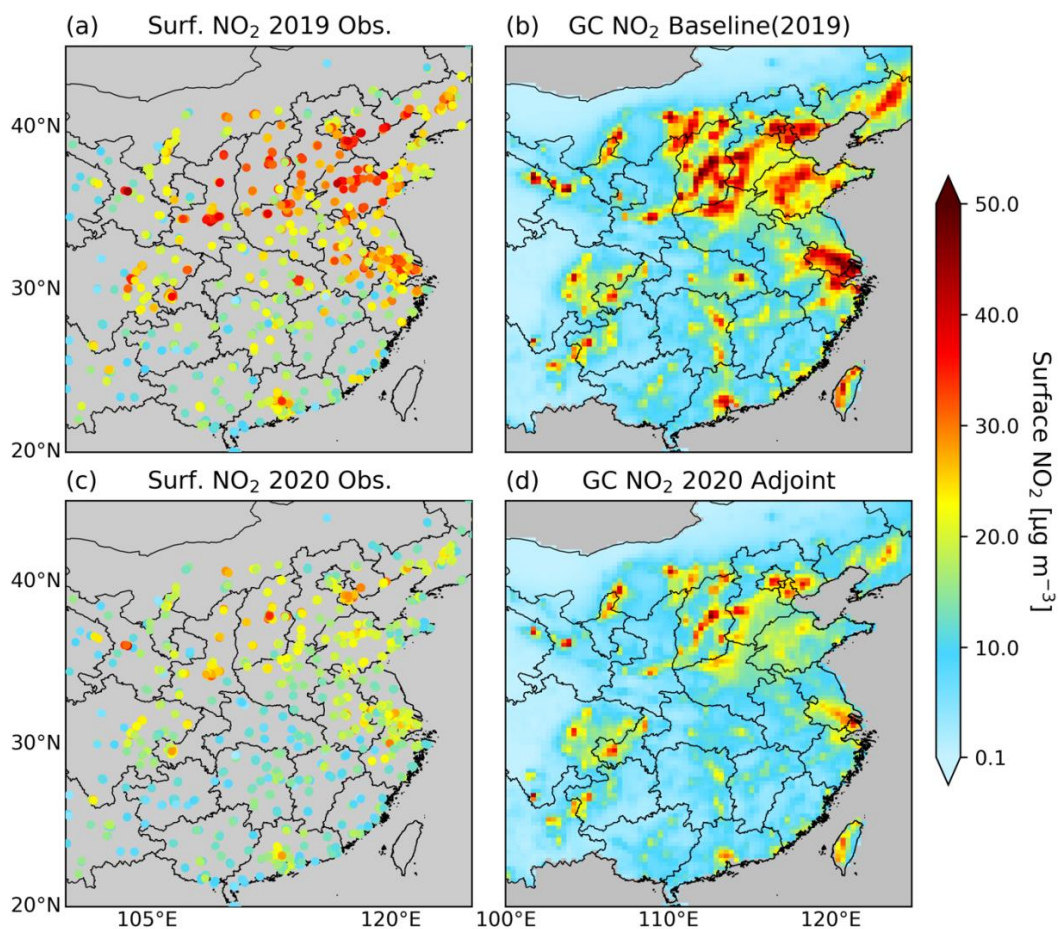
Figure 5. Comparison of surface NO$_2$ concentrations from ground measurements for (a) 2019
Feb.-Mar. and (c) 2020 Feb.-Mar. versus those from GEOS-Chem simulations (b) Baseline (2019)
and (d) 2020 Adjoint. Grey color means no data is presented.
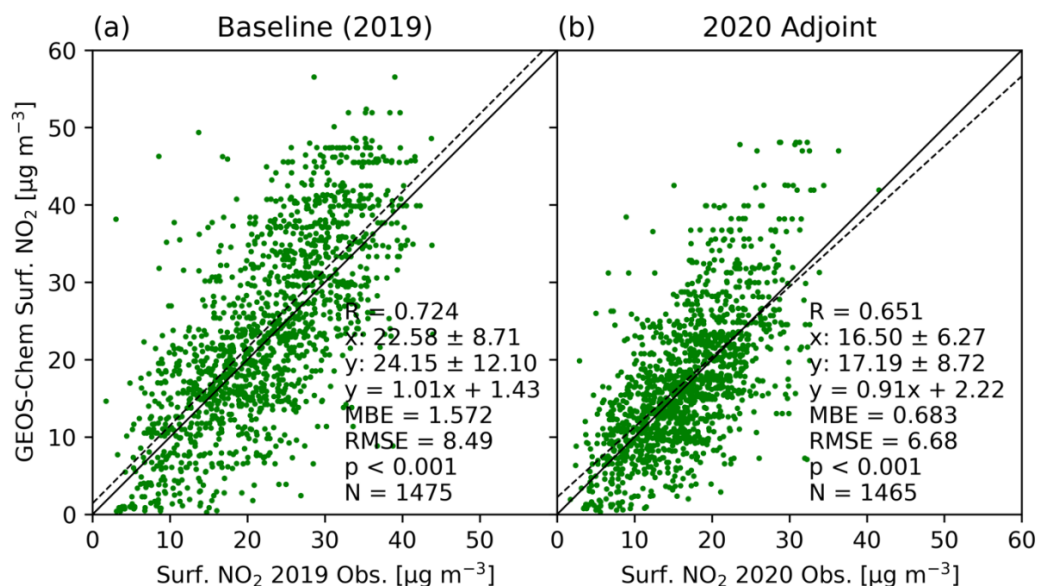
Figure 6. Scatter plots for comparing the surface NO₂ concentrations from GEOS-Chem simulations and ground measurements. (a) GEOS-Chem simulation Baseline (2019) versus ground measurements in 2019 Feb.-Mar. (b) GEOS-Chem simulation 2020 Adjoint versus ground measurements in 2020 Feb.-Mar. Note: the number of ground sites differ in these two years.

Table 2. Evaluation statistics for modeled surface NO₂ compared with the in-situ measurements*.

Experiments	R	MBE ($\mu g\ m^{-3}$)	RMSE ($\mu g\ m^{-3}$)	Slope	Intercept ($\mu g\ m^{-3}$)
Baseline (2019)	0.724	1.572	8.49	1.01	1.43
2020 Default	0.661	6.021	10.43	1.19	2.95
2020 NOx	0.608	1.726	7.74	0.92	3.03
2020 Adjoint	0.651	0.683	6.68	0.91	2.22

* The simulation experiment Baseline (2019) is compared with the ground measurements in 2019 Feb.-Mar. Other three experiments are compared with the ground measurements in 2020 Feb.-Mar.

Fig. 7 (a) is the Taylor diagram for evaluating the GEOS-Chem simulations of surface NO₂ concentrations from 2020 Default, 2020 NOx and 2020 Adjoint using the in-situ measurements.

375   The simulation 2020 Adjoint (inverted triangle in Fig. 7(a)) has the best performance among these

376   three simulations with the lowest relative bias and lowest normalized centered RMSE. Without

377   updating the NOx emission, 2020 Default features a relative bias of ~37%. After updating the NOx

378   emissions, 2020 NOx reduces the relative bias, normalized centered RMSE and normalized

379   standard deviation from around 37%, 1.38 and 1.80 to around 10%, 1.20 and 1.51 compared with

380   2020 Default, but the correlation coefficient also decreases. By using 4D-Var method, 2020

381   Adjoint further reduces the relative bias, normalized centered RMSE and normalized standard

382   deviation and increases the correlation coefficient compared with 2020 NOx.
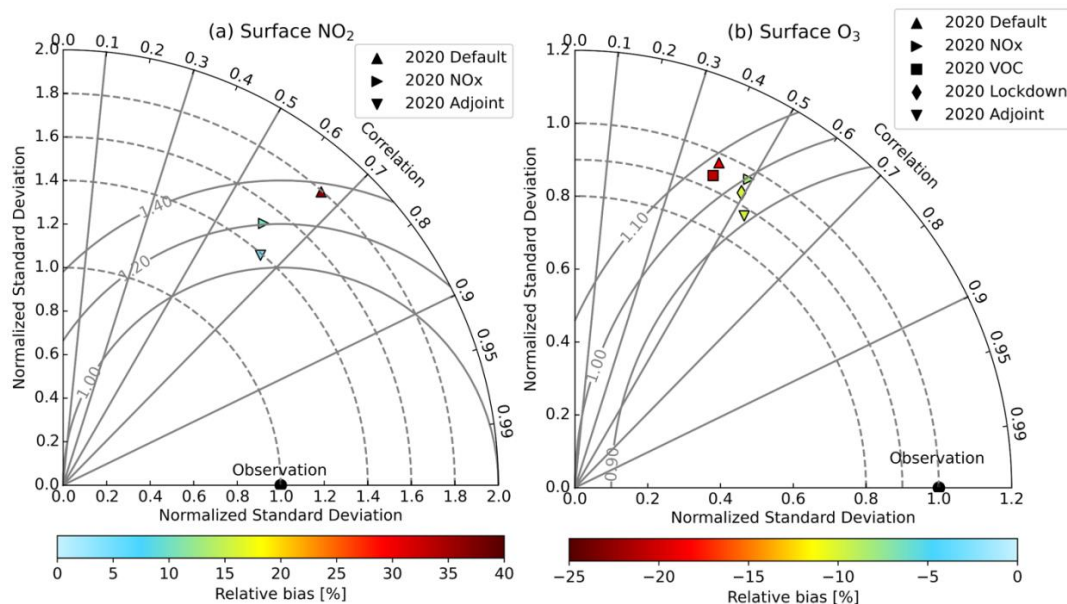
383

384   **Figure 7.** Taylor diagram for evaluating the GEOS-Chem simulations of (a) surface NO_2 and (b)

385   surface O_3 during lockdown period (2020 Feb.-Mar.) using ground observations for different

386   simulation experiments listed in Table 1. The evaluation of surface O_3 only includes the areas

387   where the NOx emissions optimized by 4D-Var reduced by more than 10%.

388

389

390   **3.3 Evaluation of surface O_3 simulations**

391   We evaluated the GEOS-Chem simulations of MDA8 surface O_3 from different simulation

392   experiments listed in Table 1 using ground measurements. Fig. 7(b) is the Taylor diagram for

393   comparing the surface O_3 concentrations during 2020 Feb.-Mar. from ground measurements and

394 GEOS-Chem simulations. We focused on areas with significant NOx emissions reduction to better

395 assess the role of updated NOx emissions in improving surface O_3 simulations. The ground sites

396 where the NOx emissions from 4D-Var decline by less than 10% are excluded. The correlation

397 coefficient between the simulation Baseline (2019) and ground observations is ~0.53 and the

398 relative bias is around -25%. By applying 2020 meteorological fields and scaling the VOC

399 emissions, the correlation coefficients decreased to ~0.40 for model simulations 2020 Default and

400 2020 VOC, with little reduction in the relative bias. By updating the NOx emissions, the relative

401 bias reduced to around -10% while the correlation coefficients remain at ~0.50 for model

402 simulations 2020 NOx, 2020 Lockdown and 2020 Adjoint. This indicates the NOx emission

403 updates significantly improve the surface O_3 simulations. Comparing the simulations 2020 Default

404 and 2020 VOC, or 2020 NOx and 2020 Lockdown, the results show that scaling VOC emissions

405 does not improve the surface O_3 simulations significantly over the continental China, but over

406 South China, VOC emissions update reduces the relative bias by 3%. Among all simulations, 2020

407 Adjoint exhibits the best performance with the lowest normalized centered RMSE, largest

408 correlation coefficient and a low relative bias of ~10%. This result further confirms the superiority

409 of the 4D-Var with respect to the mass balance method for optimizing NOx emissions. Therefore,

410 we used the 2020 Adjoint to evaluate the impacts of NOx emission on surface O_3 in the following

411 analysis.

412   Fig. 8 compares the modeled surface O_3 in Feb.-Mar. of 2019 (Fig. 8(a)) and 2020 (Fig.

413 8(b)) and the relative difference (Fig. 8(c)) computed from Equation (6) with the in-situ

414 measurements (Fig. 8(d-f)). The ground observations show that the highest level of surface O_3

415 pollution occurs in North China and southwest of China. The average MDA8 O_3 in two months

416 can reach up to ~110 μg m^{-3} at STP (~51.4 ppbv), which is higher than the China National Ambient

417 Air Quality Standard daily maximum 8-hour Grade I standard of 100 μg m^{-3}. GEOS-Chem model

418 underestimates the surface O_3 over North China for both years compared with ground observations,

419 which could be a result of the out-of-date VOC emissions, but it captures the magnitude and spatial

420 distribution of surface O_3 and the increasing trend in South China well. In South China, the

421 measured surface O_3 in 2020 Feb.-Mar. increases by 30-50%, while over North China, it increases

422 generally by less than 20% even decreases in some regions. The relative differences of simulated

423 surface O_3 between two years is comparable to the ground observations over South China (green

424 box in Fig. 8(c, f)). Over North China (pink box in Fig. 8(c, f)), the average relative difference

between two years from the model and observation are 4.27% and -3.01%, respectively, both of which are much smaller than their counterparts in South China. While the relative difference from model simulations has different signs as compared to that of observations on average, both the change of O_3 is indeed small and the model is able to capture the part of O_3 decrease in the southwest part of the North China domain (Fig. 8(c)). We note that some previous studies showed large increase of O_3 in North China, but such increase is in comparison with the O_3 in the month right before the lockdown (not the same time in 2019; (Shi & Brasseur, 2020; Y. M. Liu et al., 2021).
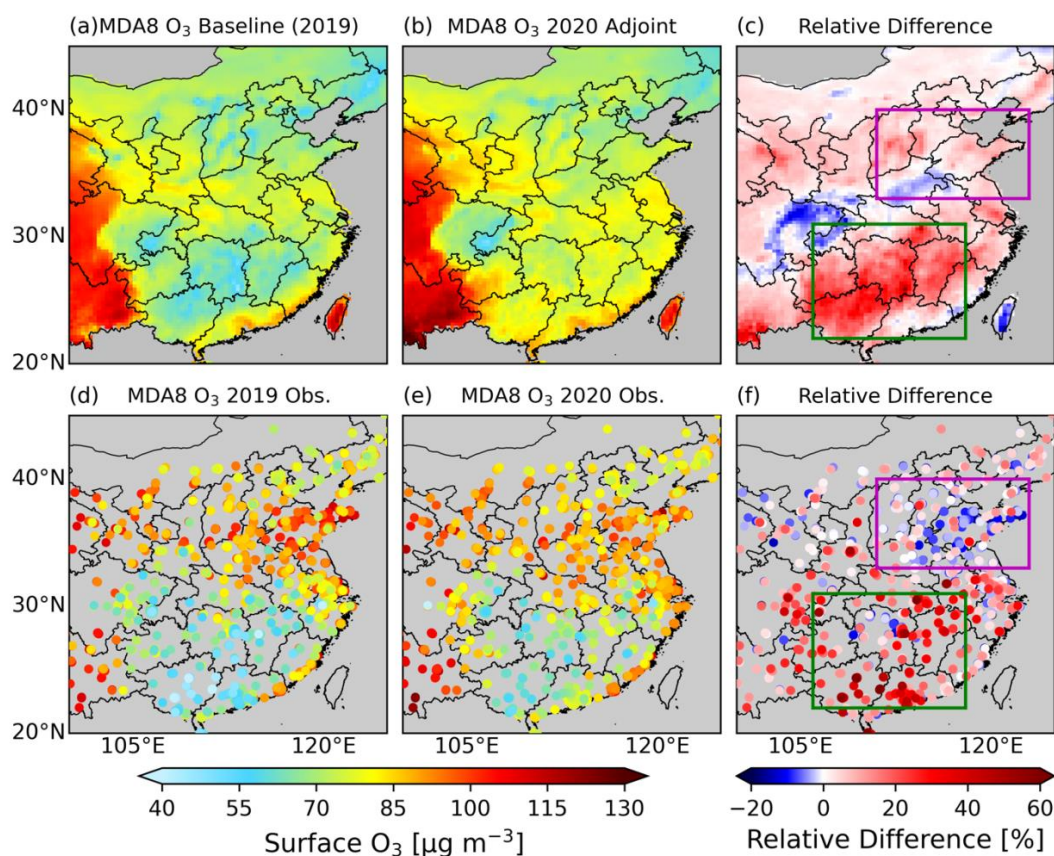
Figure 8. Comparison of MDA8 surface O_3 in 2019 and 2020 Feb.-Mar. and the relative difference between two years from GEOS-Chem model (a-c) versus ground observations (d-f). GEOS-Chem mean MDA8 O_3 at 9 m above the surface under standard temperature and pressure (STP; 273.15

438   K, 101.325 kPa) from (a) Baseline (2019) and (b) 2020 Adjoint simulation (Table 1) together with

439   (c) their relative difference. Ground observed mean MDA8 surface O3 under STP in (d) 2019 Feb.-

440   Mar.; (e) 2020 Feb.-Mar. and (f) their relative difference. The pink and green boxes in (c) and (f)

441   define the North China and South China domain.

442

443

4. Mechanism of aggravated surface O$_3$ pollution

4.1 Relative contribution from declining emissions and meteorological variations

446   From equations (2)-(5) we can analyze the mechanism of surface O$_3$ increase in China

447   during the COVID-19 pandemic (Fig. 9). NOx emission reduction as a result of COVID-19

448   lockdown leads to a ~8% increase in the mean MDA8 surface O$_3$ over North China (pink boxes in

449   Fig. 9) between 2019 and 2020 Feb.-Mar. (Fig. 9(a)), while the VOC emission decline causes ~3%

450   of O$_3$ decrease (Fig. 9(b)). The average contribution of the meteorological variations to the surface

451   O$_3$ change is less than 1% in North China (Fig. 9(d)). However, in South China, the inter-annual

452   meteorological variations dominate the surface O$_3$ increases, causing a ~30% increase (Fig. 9(d)),

453   while the NOx and VOC emission reduction has little impacts. The overall magnitude of emissions

454   contribution to the surface O$_3$ change over North China is ~5%, similar to that of the

455   meteorological effects, but meteorological variations lead to both O$_3$ increases and decreases in

456   different regions. Over South China, the meteorological effect is much larger than the net effects

457   of declining emissions. Overall, the impact of inter-annual meteorological variations between 2019

458   and 2020 is almost 30 times larger than the overall emissions impacts on the aggregated surface

459   O$_3$ pollution in China. Our results are consistent with the conclusion from Zhao et al. (2020) that

460   meteorological variation has larger impacts than emissions reduction on surface O$_3$ in the southern

461   city of Guangzhou, but in Beijing, emission reduction has a larger impact during 23-29 January.

462   Liu et al. (2020b) reported that the surface O$_3$ increase in the major cites of the Yangtze River

463   Delta region were driven by both emission reduction and meteorological variations to a similar

464   degree from pre-lockdown period (Jan. 1-22, 2020) to lockdown period (Jan. 23-Feb. 29, 2020).

465   However, Zhao et al. (2020) and Liu et al. (2020b) only focused on the lockdown period of one

466   week in reference to the time period right before the lockdown instead of the same period in

467   previous years, which cannot exclude the effects of seasonal variation of meteorology and did not

468   provide a comprehensive analysis over the whole lockdown period. Moreover, Liu et al. (2020b)

469   only analyzed four representative cities instead of showing the analysis at a national scale. Further,

470   Zhao et al. (2020) did not update the anthropogenic emissions during the lockdown period, which

471   brings significant uncertainties to their analysis.

472

473
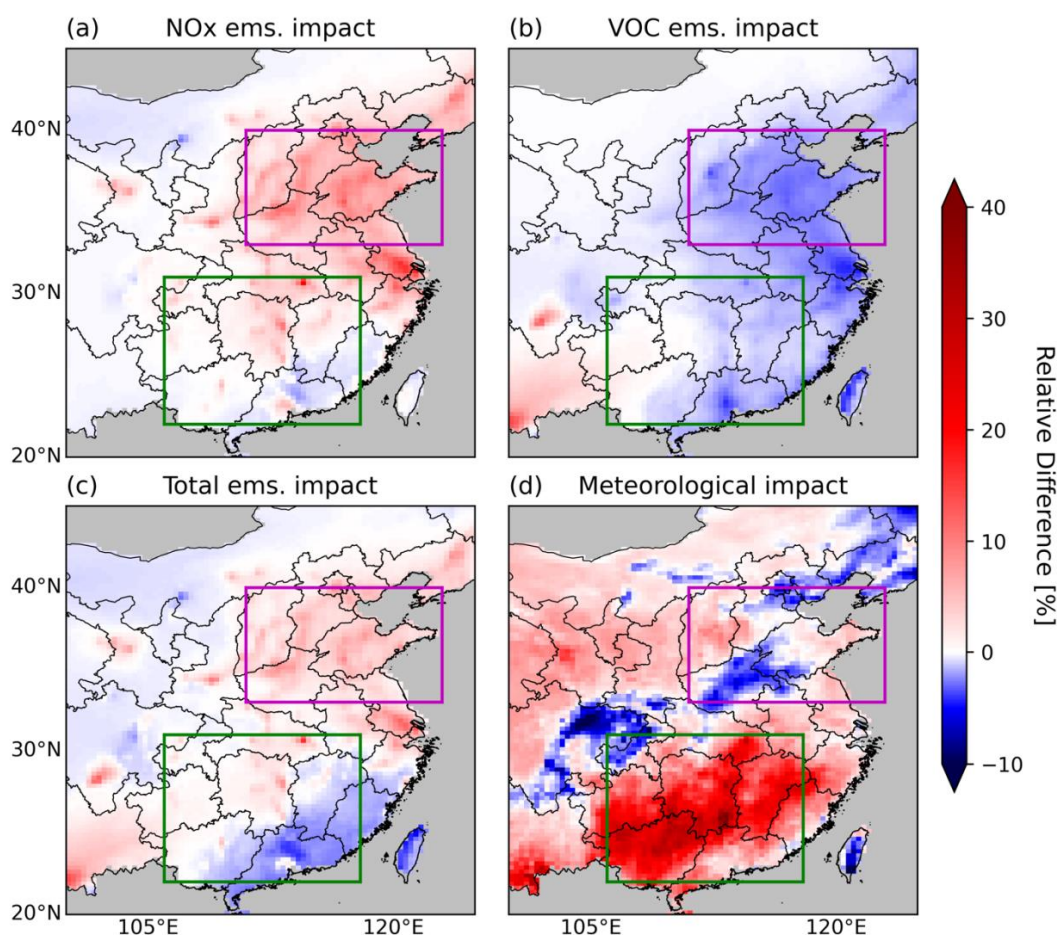
474

475   **Figure 9.** Relative difference in simulated surface O$_3$ caused by (a) NOx emission reduction, (b)

476   VOC emission reduction, (c) overall emission reduction and (d) meteorological variations due to

477   COVID-19 lockdown. The pink and green boxes in each panel define the North China and South

478   China domain.

479

480

4.2 Higher temperature leading to aggravated surface O₃ pollution in South China

The positive correlation between the surface O_3 and temperature is widely observed and reported in the literature (Pusede et al., 2015). Higher temperature leads to higher concentrations of surface O_3 because it improves the O_3 production rate by affecting the organic reactivity, production of HOx radicals, formation and decomposition of peroxy nitrates and alkyl nitrates (Pusede et al., 2015). We calculated the daily difference in Feb.-Mar. between 2020 and 2019 (excluding Feb. 29, 2020) for the daily mean of MDA8 O_3 from ground measurements and 2-meter air temperature from GEOS-FP data used in our GEOS-Chem simulations for the South China (106°E - 118°E, 22°N - 31°N, green box in Fig. 10(a)) and North China (111°E - 123°E, 33°N - 40°N, pink box in Fig. 10(a)). Fig. 10 displays the difference of 2-month mean 2-meter air temperature in Feb.-Mar. between 2020 and 2019 (Fig. 10(a)) and the scatter plot between the daily difference of measured surface O_3 concentration and 2-meter air temperature over both South China (green dots in Fig. 10(b)) and North China (pink dots in Fig. 10(b)). We found the 2-meter air temperature increased by ~2.3°C in South China, and the daily difference of surface O_3 concentration and 2-meter air temperature are well correlated with a positive correlation coefficient of 0.612. Therefore, the significant aggravated surface O_3 pollution in South China could be attributed to the temperature increase. The reason for the temperature increase is the lower cloud fraction. Via analyzing the GEOS-FP data, we found the cloud fraction decreases by ~5%, and the downward visible direct flux at surface increased by 5 W m^{-2} over South China. The lower cloud fraction increases the downward solar radiation at the surface during the lockdown period, leading to higher surface air temperature. The enhanced solar radiation at the surface could also promote the production of O_3 via photochemical reactions. In North China, 2-meter air temperature also increased by 1.8°C, but the measured surface MDA8 O_3 decreased by 3% (Fig. 8(f)). Fig. 10(b) shows the daily difference of MDA8 O_3 and 2-meter air temperature over North China also has a high correlation coefficient of 0.731. However, the intercept of the linear regression line is negative, so that the surface O_3 could decrease even though the temperature increases. The predicted average change of surface MDA8 O_3 in South China and North China are marked by the green and pink open squares respectively in Fig. 10(b) based on the linear regression. Because of the different intercepts, the predicted MDA8 O_3 in South China increases by ~9.0 µg m^{-3}, while it decrease by 2.2 µg m^{-3} in North China, although the average temperature increased in both South and North China.

512

513
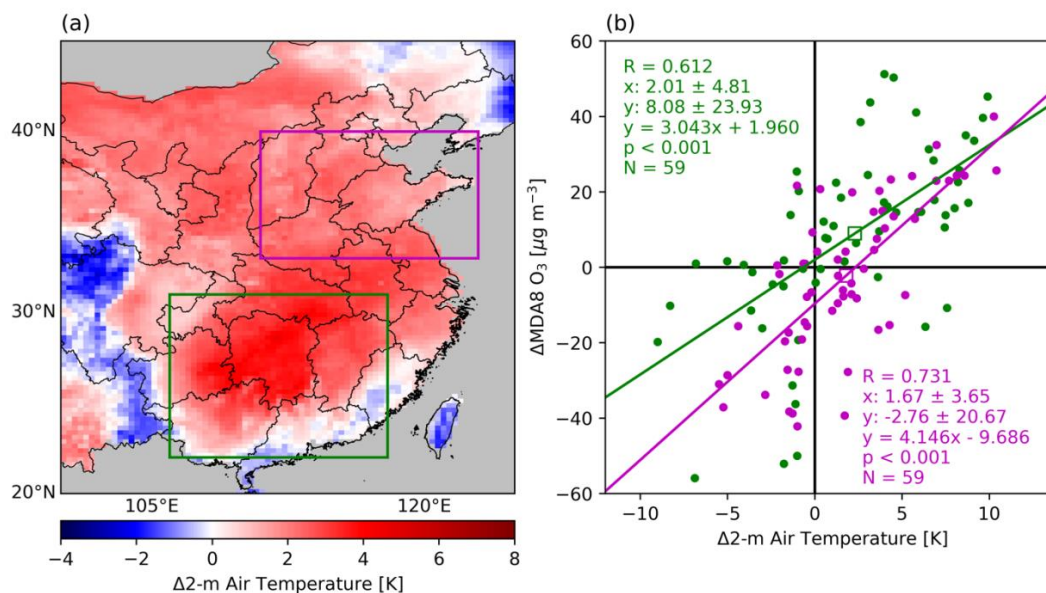
Figure 10. (a) The change of 2-meter air temperature from 2019 Feb.-Mar. to 2020 Feb.-Mar. (b)
The scatter plots between the daily difference of surface O_3 measurements and 2-meter air
temperature in Feb.-Mar. between 2020 and 2019 over South China (green dots) and North China
(pink dots). The green and pink open squares mark the predicted average change of surface MDA8
O_3 in South China (green open square) and North China (pink open square), respectively, based
on the linear regression against temperature change.

520

5. Summary

A significant reduction in primary air pollutants has been identified by surface and satellite
observations during the COVID-19 pandemic in China (Bauwens et al., 2020; Miyazaki et al.,
2020), which is in contrast to the increase of surface O_3. In this study, we analyzed the reasons for
the enhanced surface O_3 pollution from two perspectives: anthropogenic emissions reduction and
inter-annual meteorological variations. We constrain the NOx emissions based on the TROPOMI
NO_2 product using both the mass balance and 4D-Var methods. The VOC emissionw were also
updated based on the TROPOMI HCHO product via the mass balance approach. We analyzed the
contributions from emissions reduction and meteorological variations to surface O_3 increases
through a series of sensitivity simulations using the GEOS-Chem model.

531   The updated NOx emissions from the 4D-Var and mass balance approaches share a similar

532   spatial pattern. However, the NOx emissions from 4D-Var are lower than those from the mass

533   balance method over North China by ~10% but larger over central China by ~40%. The evaluation

534   of the simulations with the updated emissions against the TROPOMI NO_2, in-situ measurements

535   of surface NO_2 and O_3 indicate that the NOx emissions from the 4D-Var inversion leads to better

536   model performance than that from the mass balance approach.

537   The anthropogenic NOx emission decreased by ~30% over East China during 2020 Feb.-

538   Mar. compared to the same period in 2019. Over North China, NOx emission reduction leads to a

539   ~8% increase in the mean MDA8 surface O_3, while the VOC emissions decline causes O3 to

540   decrease by ~3%. The average contribution of meteorological variations to the surface O_3 change

541   is less than 1% in North China. However, in South China, the inter-annual meteorological variation

542   dominates the surface O_3 increase, causing a ~30% increase, while the NOx and VOC emission

543   reduction has nearly no impacts on O_3. Overall, the impact of inter-annual meteorological

544   variations between 2019 and 2020 is almost 30 times larger than the impact of emissions on the

545   enhanced surface O_3 pollution in China.

546   The significant increase of surface O_3 in South China could be attributed to the higher

547   temperature during the lockdown period, which is caused by the lower cloud fraction. The lower

548   cloud fraction increases the downward solar radiation at the surface during the lockdown period,

549   leading to higher surface air temperature. The enhanced solar radiation at the surface could also

550   promote the production of O_3 via photochemical reactions.

551

552

553   Appendix A: NOx emission reduction in China from 2010 to 2019

554   The default anthropogenic NOx emission over East Asia in GEOS-Chem is MIX 2010 (Li

555   et al., 2017).To generate the anthropogenic NOx emission in 2019, we calculated the ratio of mean

556   TROPOMI tropospheric NO_2 VCD in Feb.-Mar. 2019 to GEOS-Chem simulated NO_2 VCD with

557   the default MIX 2010 emission as the scaling factor (Fig. A1). The scaling factors in regions where

558   mean TROPOMI tropospheric NO_2 VCD in 2019 Feb.-Mar. less than 0.1 DU are set to 1. From

559   2010 to 2019, the anthropogenic NOx emission has declined significantly as a result of the clean

560   air actions of Chinese government (Zheng et al., 2018).

561

562
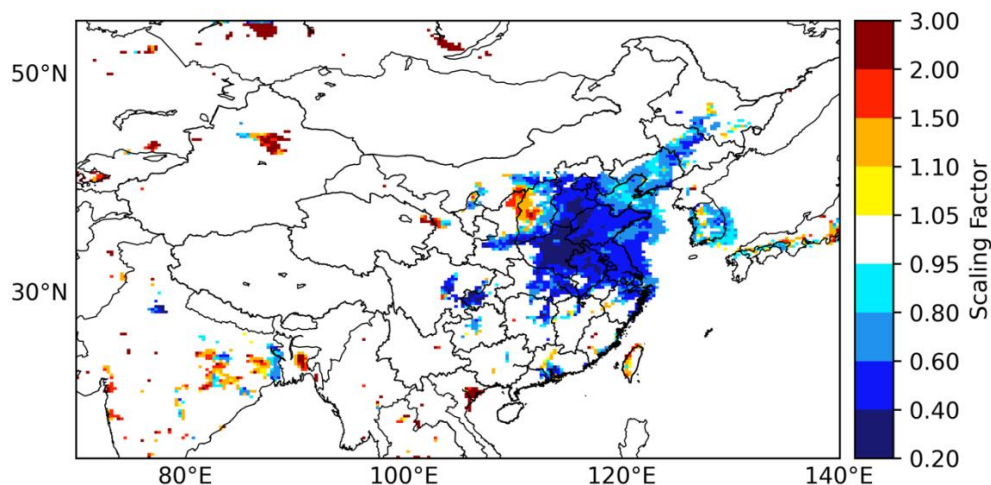
Figure A1. The scaling factor of anthropogenic NOx emission from year 2010 to 2019.

564

565

566 **Appendix B: Applying the TROPOMI NO₂ averaging kernel in the observation**

567 **operator**

568   To optimize the NOx emissions and minimize the cost function (Equation (1)) with the 4D-

569 Var method, GEOS-Chem adjoint needs to compute the derivative of the cost function with respect

570 to the model parameters to be optimized, which is the scaling factors of the anthropogenic NOx

571 emissions in this study. An essential step is to calculate the adjoint forcing $\boldsymbol{F}$, which is the

572 derivative of the cost function with respect to the modeled NO₂ concentration shown as Equation

573 (B1).

574
$$\boldsymbol{F} = \frac{\partial J}{\partial \boldsymbol{c}} = \boldsymbol{S}_{\mathrm{obs}}^{-1}[H(\boldsymbol{c}) - \boldsymbol{s}]\frac{\partial H(\boldsymbol{c})}{\partial \boldsymbol{c}} \tag{B1}$$

575 For each single TROPOMI NO₂ observation, the adjoint forcing component f and cost function

576 component j are computed as Equation (B2) and Equation (B3).

577
$$f = \frac{M_{\mathrm{gc}}v_{\mathrm{gc}} - M_{\mathrm{obs}}v_{\mathrm{obs}}}{e_{\mathrm{obs}}M_{\mathrm{obs}}}M_{\mathrm{gc}} \tag{B2}$$

578
$$j = \frac{0.5f\left(M_{\mathrm{gc}}v_{\mathrm{gc}} - M_{\mathrm{obs}}v_{\mathrm{obs}}\right)}{M_{\mathrm{gc}}} \tag{B3}$$

579   Here M_{gc} is GEOS-Chem air mass factor applying the GEOS-Chem NO₂ vertical profiles and

580   TROPOMI NO₂ averaging kernel. M_{obs} is TROPOMI air mass factor. v_{gc} and v_{obs} are the

581   tropospheric NO₂ VCD from GEOS-Chem model and TROPOMI observation, respectively. The

582   product of air mass factor and NO₂ VCD is NO₂ slant column density. e_{obs} is the standard error of

583   TROPOMI tropospheric NO₂ VCD.

584   We calculated the GEOS-Chem air mass factor M_{gc} as Equation (B4) following Qu et al.

585   (2019).

586
$$M_{gc} = \frac{\sum_{i \in \text{trop.}} c_i^{gc} \Delta p_i^{gc} w_i^{gc}}{\sum_{i \in \text{trop.}} c_i^{gc} \Delta p_i^{gc}} \tag{B4}$$

587   Here c_i^{gc} is GEOS-Chem NO₂ mixing ratio at vertical layer i, Δp_i^{gc} is the pressure difference

588   between the GEOS-Chem vertical layer i and $i+1$. w_i^{gc} is the scattering weight at the GEOS-Chem

589   vertical layer i, which is calculated by the linear interpolation of the scattering weights at the

590   vertical coordinate of the model TM5 used for TROPOMI NO₂ retrieval. The scattering weight at

591   the TM5 vertical layer l (w_l^{TM5}) is computed as the product of TROPOMI air mass factor and the

592   TROPOMI averaging kernel at the TM5 vertical layer l (A_l^{TM5}) using Equation (B5) (Eskes and

593   Boersma, 2003).

594
$$w_l^{TM5} = M_{obs} A_l^{TM5} \tag{B5}$$

595

Appendix C: Validation of the TROPOMI NO₂ observation operator

597   We validated the observation operator by comparing the sensitivity of the cost function

598   with respect to the emission scaling factor from GEOS-Chem adjoint and a finite difference

599   estimation as shown in Equation (C1). We shut down the transport and exclude a priori term from

600   the cost function for the validation, so that the gradient of cost function component in each grid

601   cell to the local emission scaling factor equals to the gradient of total cost function to the emission

602   scaling factor in the same grid cell.

603
$$\frac{\partial J(\ln \sigma)}{\partial \ln \sigma} \approx \frac{J(\ln(\sigma + 0.05)) - J(\ln(\sigma - 0.05))}{\ln(\sigma + 0.05) - \ln(\sigma - 0.05)} \tag{C1}$$

604   Fig. C1 compared the cost function sensitivities calculated from GEOS-Chem adjoint and

605   the finite difference method for the nested grids with the spatial resolution of 0.25°×0.3125°. The

606   spatial pattern and magnitude of the cost function sensitivities from the two methods match with

607   each other with a correlation coefficient of 0.97. The statistics show that the agreement of the
608   adjoint sensitivities and finite difference sensitivities in this study is comparable to that in Wang
609   et al. (2020a) although we constrain the NOx emission at a much finer resolution of 0.25°×0.3125°
610   than in their study (2°×2.5°).
611
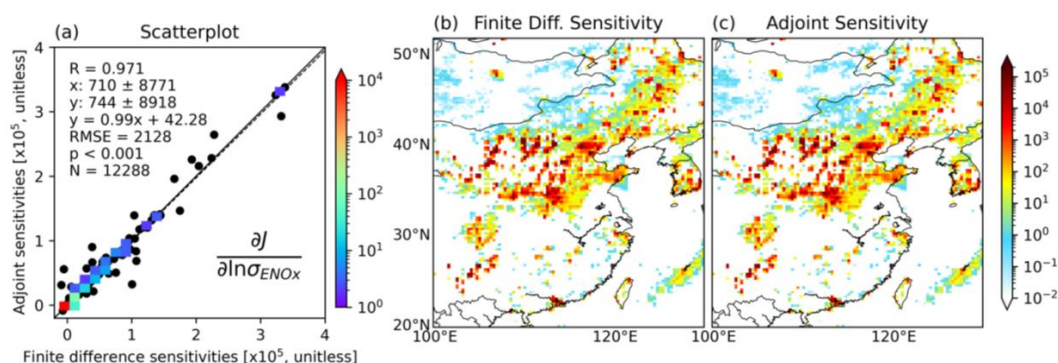
612

613   **Figure C1.** Comparison of adjoint sensitivities and finite difference sensitivities. (a) Scatter plot
614   of the adjoint sensitivity of the cost function with respect to the logarithm of NOx emission scaling
615   factor versus the finite difference sensitivities. The color scheme for panel (a) encodes the number
616   of samples (the legend on the right of panel (a)). (b) Map of finite difference sensitivity. (c) Map
617   of adjoint sensitivity.
618

619

620   **Data availability**

621   The TROPOMI NO$_2$ and HCHO product are available at the NASA Goddard Earth
622   Sciences Data and Information Services Center (https://daac.gsfc.nasa.gov). The ground O$_3$ and
623   NO$_2$ measurements are available at the China National Environmental Monitoring Center
624   (http://www.cnemc.cn/en/).
625

626   **Author contribution**

627   ZL and JW designed the research, and ZL conducted the research. YW, DKH and XC
628   contributed to the research design. ZL and JW wrote the manuscript, and XC and DKH contributed
629   to the writing. YW and TS developed the codes for comparing the tropospheric NO$_2$ VCD from
630   model and TROPOMI data. KS developed the codes for oversampling.

631

Competing interests

633   The authors declare that they have no conflict of interest.

634

Acknowledgements

636   This research is supported by the NASA ACMAP program (grant number: 80NSSC19K0950). We acknowledge the computational support from the High-Performance Computing group at the University of Iowa.

639

640

641

References

Bauwens, M., Compernolle, S., Stavrakou, T., Muller, J. F., van Gent, J., Eskes, H., Levelt, P. F., van der A, R., Veefkind, J. P., Vlietinck, J., Yu, H., and Zehner, C.: Impact of Coronavirus Outbreak on NO2 Pollution Assessed Using TROPOMI and OMI Observations, Geophys Res Lett, 47, 10.1029/2020GL087978, 2020.

Bey, I., Jacob, D. J., Yantosca, R. M., Logan, J. A., Field, B. D., Fiore, A. M., Li, Q., Liu, H. Y., Mickley, L. J., and Schultz, M. G.: Global modeling of tropospheric chemistry with assimilated meteorology: Model description and evaluation, Journal of Geophysical Research: Atmospheres, 106, 23073-23095, 10.1029/2001jd000807, 2001.

Bi, Z., Ye, Z., He, C., and Li, Y.: Analysis of the meteorological factors affecting the short-term increase in O3 concentrations in nine global cities during COVID-19, Atmospheric Pollution Research, 13, 101523, https://doi.org/10.1016/j.apr.2022.101523, 2022.

Chen, D., Wang, Y., McElroy, M. B., He, K., Yantosca, R. M., and Le Sager, P.: Regional CO pollution and export in China simulated by the high-resolution nested-grid GEOS-Chem model, Atmospheric Chemistry and Physics, 9, 3825-3839, 10.5194/acp-9-3825-2009, 2009.

Cooper, M., Martin, R. V., Padmanabhan, A., and Henze, D. K.: Comparing mass balance and adjoint methods for inverse modeling of nitrogen dioxide columns for global nitrogen oxide emissions, Journal of Geophysical Research: Atmospheres, 122, 4718-4734, 10.1002/2016jd025985, 2017.

661 De Smedt, I., Theys, N., Yu, H., Danckaert, T., Lerot, C., Compernolle, S., Van Roozendael, M.,
662 Richter, A., Hilboll, A., Peters, E., Pedergnana, M., Loyola, D., Beirle, S., Wagner, T., Eskes, H.,
663 van Geffen, J., Boersma, K. F., and Veefkind, P.: Algorithm theoretical baseline for formaldehyde
664 retrievals from S5P TROPOMI and from the QA4ECV project, Atmospheric Measurement
665 Techniques, 11, 2395-2426, 10.5194/amt-11-2395-2018, 2018.

666 Eskes, H. J. and Boersma, K. F.: Averaging kernels for DOAS total-column satellite retrievals,
667 Atmospheric Chemistry and Physics, 3, 1285-1291, 10.5194/acp-3-1285-2003, 2003.

668 Ghahremanloo, M., Lops, Y., Choi, Y., and Mousavinezhad, S.: Impact of the COVID-19 outbreak
669 on air pollution levels in East Asia, Science of the Total Environment, 754,
670 10.1016/j.scitotenv.2020.142226, 2021.

671 Gong, C., Lei, Y., Ma, Y., Yue, X., and Liao, H.: Ozone–vegetation feedback through dry
672 deposition and isoprene emissions in a global chemistry–carbon–climate model, Atmos. Chem.
673 Phys., 20, 3841-3857, 10.5194/acp-20-3841-2020, 2020.

674 Guenther, A. B., Jiang, X., Heald, C. L., Sakulyanontvittaya, T., Duhl, T., Emmons, L. K., and
675 Wang, X.: The Model of Emissions of Gases and Aerosols from Nature version 2.1 (MEGAN2.1):
676 an extended and updated framework for modeling biogenic emissions, Geoscientific Model
677 Development, 5, 1471-1492, 10.5194/gmd-5-1471-2012, 2012.

678 Guo, J., Zhang, X. S., Gao, Y., Wang, Z. W., Zhang, M. G., Xue, W. B., Herrmann, H., Brasseur,
679 G. P., Wang, T., and Wang, Z.: Evolution of Ozone Pollution in China: What Track Will It Follow?,
680 Environmental Science & Technology, 57, 109-117, 10.1021/acs.est.2c08205, 2023.

681 Henze, D. K., Hakami, A., and Seinfeld, J. H.: Development of the adjoint of GEOS-Chem,
682 Atmospheric Chemistry and Physics, 7, 2413-2433, 10.5194/acp-7-2413-2007, 2007.

683 Henze, D. K., Seinfeld, J. H., and Shindell, D. T.: Inverse modeling and mapping US air quality
684 influences of inorganic PM2.5 precursor emissions using the adjoint of GEOS-Chem, Atmospheric
685 Chemistry and Physics, 9, 5877-5903, 10.5194/acp-9-5877-2009, 2009.

686 Hoesly, R. M., Smith, S. J., Feng, L., Klimont, Z., Janssens-Maenhout, G., Pitkanen, T., Seibert,
687 J. J., Vu, L., Andres, R. J., Bolt, R. M., Bond, T. C., Dawidowski, L., Kholod, N., Kurokawa, J.-
688 i., Li, M., Liu, L., Lu, Z., Moura, M. C. P., O'Rourke, P. R., and Zhang, Q.: Historical (1750–2014)
689 anthropogenic emissions of reactive gases and aerosols from the Community Emissions Data
690 System (CEDS), Geoscientific Model Development, 11, 369-408, 10.5194/gmd-11-369-2018,
691 2018.

692 Huang, X., Ding, A., Gao, J., Zheng, B., Zhou, D., Qi, X., Tang, R., Wang, J., Ren, C., Nie, W.,

693 Chi, X., Xu, Z., Chen, L., Li, Y., Che, F., Pang, N., Wang, H., Tong, D., Qin, W., Cheng, W., Liu,

694 W., Fu, Q., Liu, B., Chai, F., Davis, S. J., Zhang, Q., and He, K.: Enhanced secondary pollution

695 offset reduction of primary emissions during COVID-19 lockdown in China, National Science

696 Review, 8, 10.1093/nsr/nwaa137, 2020.

697 Hudman, R. C., Moore, N. E., Mebust, A. K., Martin, R. V., Russell, A. R., Valin, L. C., and

698 Cohen, R. C.: Steps towards a mechanistic model of global soil nitric oxide emissions:

699 implementation and space based-constraints, Atmospheric Chemistry and Physics, 12, 7779-7795,

700 10.5194/acp-12-7779-2012, 2012.

701 Janssens-Maenhout, G., Crippa, M., Guizzardi, D., Dentener, F., Muntean, M., Pouliot, G.,

702 Keating, T., Zhang, Q., Kurokawa, J., Wankmuller, R., van der Gon, H. D., Kuenen, J. J. P.,

703 Klimont, Z., Frost, G., Darras, S., Koffi, B., and Li, M.: HTAP_v2.2: a mosaic of regional and

704 global emission grid maps for 2008 and 2010 to study hemispheric transport of air pollution,

705 Atmospheric Chemistry and Physics, 15, 11411-11432, 10.5194/acp-15-11411-2015, 2015.

706 Jerrett, M., Burnett, R. T., Pope, C. A., Ito, K., Thurston, G., Krewski, D., Shi, Y. L., Calle, E.,

707 and Thun, M.: Long-Term Ozone Exposure and Mortality, New England Journal of Medicine, 360,

708 1085-1095, 10.1056/NEJMoa0803894, 2009.

709 Le, T. H., Wang, Y., Liu, L., Yang, J. N., Yung, Y. L., Li, G. H., and Seinfeld, J. H.: Unexpected

710 air pollution with marked emission reductions during the COVID-19 outbreak in China, Science,

711 369, 702-706, 10.1126/science.abb7431, 2020.

712 Leue, C., Wenig, M., Wagner, T., Klimm, O., Platt, U., and Jähne, B.: Quantitative analysis of

713 NOx emissions from Global Ozone Monitoring Experiment satellite image sequences, Journal of

714 Geophysical Research: Atmospheres, 106, 5493-5505, 10.1029/2000jd900572, 2001.

715 Levelt, P. F., Zweers, D. C. S., Aben, I., Bauwens, M., Borsdorff, T., De Smedt, I., Eskes, H. J.,

716 Lerot, C., Loyola, D. G., Romahn, F., Stavrakou, T., Theys, N., Van Roozendael, M., Veefkind, J.

717 P., and Verhoelst, T.: Air quality impacts of COVID-19 lockdown measures detected from space

718 using high spatial resolution observations of multiple trace gases from Sentinel-5P/TROPOMI,

719 Atmospheric Chemistry and Physics, 22, 10319-10351, 10.5194/acp-22-10319-2022, 2022.

720 Li, M., Zhang, Q., Kurokawa, J.-i., Woo, J.-H., He, K., Lu, Z., Ohara, T., Song, Y., Streets, D. G.,

721 Carmichael, G. R., Cheng, Y., Hong, C., Huo, H., Jiang, X., Kang, S., Liu, F., Su, H., and Zheng,

722 B.: MIX: a mosaic Asian anthropogenic emission inventory under the international collaboration

framework of the MICS-Asia and HTAP, Atmospheric Chemistry and Physics, 17, 935-963, 10.5194/acp-17-935-2017, 2017.

Liu, F., Page, A., Strode, S. A., Yoshida, Y., Choi, S., Zheng, B., Lamsal, L. N., Li, C., Krotkov, N. A., Eskes, H., van der A, R., Veefkind, P., Levelt, P. F., Hauser, O. P., and Joiner, J.: Abrupt decline in tropospheric nitrogen dioxide over China after the outbreak of COVID-19, Science Advances, 6, 10.1126/sciadv.abc2992, 2020a.

Liu, S. C., Trainer, M., Fehsenfeld, F. C., Parrish, D. D., Williams, E. J., Fahey, D. W., Hubler, G., and Murphy, P. C.: Ozone production in the rural troposphere and the implications for regional and global ozone distributions, Journal of Geophysical Research-Atmospheres, 92, 4191-4207, 10.1029/JD092iD04p04191, 1987.

Liu, T., Wang, X., Hu, J., Wang, Q., An, J., Gong, K., Sun, J., Li, L., Qin, M., Li, J., Tian, J., Huang, Y., Liao, H., Zhou, M., Hu, Q., Yan, R., Wang, H., and Huang, C.: Driving Forces of Changes in Air Quality during the COVID-19 Lockdown Period in the Yangtze River Delta Region, China, Environmental Science & Technology Letters, 7, 779-786, 10.1021/acs.estlett.0c00511, 2020b.

Liu, Y. M., Wang, T., Stavrakou, T., Elguindi, N., Doumbia, T., Granier, C., Bouarar, I., Gaubert, B., and Brasseur, G. P.: Diverse response of surface ozone to COVID-19 lockdown in China, Science of the Total Environment, 789, 10.1016/j.scitotenv.2021.147739, 2021.

Lu, X., Zhang, L., Chen, Y. F., Zhou, M., Zheng, B., Li, K., Liu, Y. M., Lin, J. T., Fu, T. M., and Zhang, Q.: Exploring 2016-2017 surface ozone pollution over China: source contributions and meteorological influences, Atmospheric Chemistry and Physics, 19, 8339-8361, 10.5194/acp-19-8339-2019, 2019.

Mao, J., Paulot, F., Jacob, D. J., Cohen, R. C., Crounse, J. D., Wennberg, P. O., Keller, C. A., Hudman, R. C., Barkley, M. P., and Horowitz, L. W.: Ozone and organic nitrates over the eastern United States: Sensitivity to isoprene chemistry, Journal of Geophysical Research: Atmospheres, 118, 11,256-211,268, 10.1002/jgrd.50817, 2013.

Mao, J., Jacob, D. J., Evans, M. J., Olson, J. R., Ren, X., Brune, W. H., Clair, J. M. S., Crounse, J. D., Spencer, K. M., Beaver, M. R., Wennberg, P. O., Cubison, M. J., Jimenez, J. L., Fried, A., Weibring, P., Walega, J. G., Hall, S. R., Weinheimer, A. J., Cohen, R. C., Chen, G., Crawford, J. H., McNaughton, C., Clarke, A. D., Jaeglé, L., Fisher, J. A., Yantosca, R. M., Le Sager, P., and

753   Carouge, C.: Chemistry of hydrogen oxide radicals (HOx) in the Arctic troposphere in spring,

754   Atmospheric Chemistry and Physics, 10, 5823-5838, 10.5194/acp-10-5823-2010, 2010.

755   Martin, R. V., Jacob, D. J., Chance, K., Kurosu, T. P., Palmer, P. I., and Evans, M. J.: Global

756   inventory of nitrogen oxide emissions constrained by space-based observations of NO2 columns,

757   Journal of Geophysical Research-Atmospheres, 108, 10.1029/2003jd003453, 2003.

758   Miyazaki, K., Bowman, K., Sekiya, T., Jiang, Z., Chen, X., Eskes, H., Ru, M., Zhang, Y., and

759   Shindell, D.: Air Quality Response in China Linked to the 2019 Novel Coronavirus (COVID‐19)

760   Lockdown, Geophys Res Lett, 47, 10.1029/2020gl089252, 2020.

761   Murray, L. T., Jacob, D. J., Logan, J. A., Hudman, R. C., and Koshak, W. J.: Optimized regional

762   and interannual variability of lightning in a global chemical transport model constrained by

763   LIS/OTD satellite data, Journal of Geophysical Research: Atmospheres, 117,

764   10.1029/2012jd017934, 2012.

765   Ott, L. E., Pickering, K. E., Stenchikov, G. L., Allen, D. J., DeCaria, A. J., Ridley, B., Lin, R.-F.,

766   Lang, S., and Tao, W.-K.: Production of lightning NOx and its vertical distribution calculated from

767   three-dimensional cloud-scale chemical transport model simulations, Journal of Geophysical

768   Research, 115, 10.1029/2009jd011880, 2010.

769   Pusede, S. E., Steiner, A. L., and Cohen, R. C.: Temperature and Recent Trends in the Chemistry

770   of Continental Surface Ozone, Chemical Reviews, 115, 3898-3918, 10.1021/cr5006815, 2015.

771   Qu, Z., Henze, D. K., Capps, S. L., Wang, Y., Xu, X., Wang, J., and Keller, M.: Monthly top-down

772   NOx emissions for China (2005–2012): A hybrid inversion method and trend analysis, Journal of

773   Geophysical Research: Atmospheres, 122, 4600-4625, 10.1002/2016JD025852, 2017.

774   Qu, Z., Henze, D. K., Li, C., Theys, N., Wang, Y., Wang, J., Wang, W., Han, J., Shim, C.,

775   Dickerson, R. R., and Ren, X.: SO2 Emission Estimates Using OMI SO2 Retrievals for 2005-2017,

776   J Geophys Res Atmos, 124, 8336-8359, 10.1029/2019JD030243, 2019.

777   Sha, T., Ma, X. Y., Zhang, H. X., Janechek, N., Wang, Y. Y., Wang, Y., Garcia, L. C., Jenerette,

778   G. D., and Wang, J.: Impacts of Soil NOx Emission on O-3 Air Quality in Rural California,

779   Environmental Science & Technology, 55, 7113-7122, 10.1021/acs.est.0c06834, 2021.

780   Shi, X. and Brasseur, G. P.: The Response in Air Quality to the Reduction of Chinese Economic

781   Activities During the COVID‐19 Outbreak, Geophys Res Lett, 47, 10.1029/2020gl088070, 2020.

782 Sillman, S., Logan, J. A., and Wofsy, S. C.: The sensitivity of ozone to nitrogen-oxides and
783 hydrocarbons in regional ozone episodes, Journal of Geophysical Research-Atmospheres, 95,
784 1837-1851, 10.1029/JD095iD02p01837, 1990.

785 Steinbacher, M., Zellweger, C., Schwarzenbach, B., Bugmann, S., Buchmann, B., Ordóñez, C.,
786 Prevot, A. S. H., and Hueglin, C.: Nitrogen oxide measurements at rural sites in Switzerland: Bias
787 of conventional measurement techniques, Journal of Geophysical Research: Atmospheres, 112,
788 https://doi.org/10.1029/2006JD007971, 2007.

789 Streets, D. G., Canty, T., Carmichael, G. R., de Foy, B., Dickerson, R. R., Duncan, B. N., Edwards,
790 D. P., Haynes, J. A., Henze, D. K., Houyoux, M. R., Jacob, D. J., Krotkov, N. A., Lamsal, L. N.,
791 Liu, Y., Lu, Z., Martin, R. V., Pfister, G. G., Pinder, R. W., Salawitch, R. J., and Wecht, K. J.:
792 Emissions estimation from satellite retrievals: A review of current capability, Atmospheric
793 Environment, 77, 1011-1042, 10.1016/j.atmosenv.2013.05.051, 2013.

794 Sun, K., Zhu, L., Cady-Pereira, K., Chan Miller, C., Chance, K., Clarisse, L., Coheur, P.-F.,
795 González Abad, G., Huang, G., Liu, X., Van Damme, M., Yang, K., and Zondlo, M.: A physics-
796 based approach to oversample multi-satellite, multispecies observations to a common grid,
797 Atmospheric Measurement Techniques, 11, 6679-6701, 10.5194/amt-11-6679-2018, 2018.

798 Tong, L., Liu, Y., Meng, Y., Dai, X. R., Huang, L. J., Luo, W. X., Yang, M. R., Pan, Y., Zheng,
799 J., and Xiao, H.: Surface ozone changes during the COVID-19 outbreak in China: An insight into
800 the pollution characteristics and formation regimes of ozone in the cold season, Journal of
801 Atmospheric Chemistry, 80, 103-120, 10.1007/s10874-022-09443-2, 2023.

802 Travis, K. R., Jacob, D. J., Keller, C. A., Kuang, S., Lin, J., Newchurch, M. J., and Thompson, A.
803 M.: Resolving ozone vertical gradients in air quality models, Atmos. Chem. Phys. Discuss., 2017,
804 1-18, 10.5194/acp-2017-596, 2017.

805 Travis, K. R., Jacob, D. J., Fisher, J. A., Kim, P. S., Marais, E. A., Zhu, L., Yu, K., Miller, C. C.,
806 Yantosca, R. M., Sulprizio, M. P., Thompson, A. M., Wennberg, P. O., Crounse, J. D., St Clair, J.
807 M., Cohen, R. C., Laughner, J. L., Dibb, J. E., Hall, S. R., Ullmann, K., Wolfe, G. M., Pollack, I.
808 B., Peischl, J., Neuman, J. A., and Zhou, X.: Why do Models Overestimate Surface Ozone in the
809 Southeastern United States?, Atmos Chem Phys, 16, 13561-13577, 10.5194/acp-16-13561-2016,
810 2016.

811 van der Werf, G. R., Randerson, J. T., Giglio, L., van Leeuwen, T. T., Chen, Y., Rogers, B. M.,
812 Mu, M., van Marle, M. J. E., Morton, D. C., Collatz, G. J., Yokelson, R. J., and Kasibhatla, P. S.:

813   Global fire emissions estimates during 1997–2016, Earth System Science Data, 9, 697-720,

814   10.5194/essd-9-697-2017, 2017.

815   TROPOMI   ATBD   of   the   total   and   tropospheric   NO2   data   products:

816   https://sentinel.esa.int/documents/247904/2476257/sentinel-5p-tropomi-atbd-no2-data-products,

817   last access: Sep. 29.

818   van Geffen, J., Boersma, K. F., Eskes, H., Sneep, M., ter Linden, M., Zara, M., and Veefkind, J.

819   P.: S5P TROPOMI NO2 slant column retrieval: method, stability, uncertainties and comparisons

820   with OMI, Atmospheric Measurement Techniques, 13, 1315-1335, 10.5194/amt-13-1315-2020,

821   2020.

822   Veefkind, J. P., Aben, I., McMullan, K., Förster, H., de Vries, J., Otter, G., Claas, J., Eskes, H. J.,

823   de Haan, J. F., Kleipool, Q., van Weele, M., Hasekamp, O., Hoogeveen, R., Landgraf, J., Snel, R.,

824   Tol, P., Ingmann, P., Voors, R., Kruizinga, B., Vink, R., Visser, H., and Levelt, P. F.: TROPOMI

825   on the ESA Sentinel-5 Precursor: A GMES mission for global observations of the atmospheric

826   composition for climate, air quality and ozone layer applications, Remote Sensing of Environment,

827   120, 70-83, https://doi.org/10.1016/j.rse.2011.09.027, 2012.

828   Venter, Z. S., Aunan, K., Chowdhury, S., and Lelieveld, J.: COVID-19 lockdowns cause global

829   air pollution declines, Proceedings of the National Academy of Sciences, 117, 18984-18990,

830   doi:10.1073/pnas.2006853117, 2020.

831   Vinken, G. C. M., Boersma, K. F., van Donkelaar, A., and Zhang, L.: Constraints on ship NOx

832   emissions in Europe using GEOS-Chem and OMI satellite NO2 observations, Atmos. Chem. Phys.,

833   14, 1353-1369, 10.5194/acp-14-1353-2014, 2014.

834   Wang, Y., Wang, J., Xu, X., Henze, D. K., Qu, Z., and Yang, K.: Inverse modeling of SO_2 and

835   NO_x emissions over China using multisensor satellite data – Part 1: Formulation and sensitivity

836   analysis, Atmospheric Chemistry and Physics, 20, 6631-6650, 10.5194/acp-20-6631-2020, 2020a.

837   Wang, Y., Wang, J., Zhou, M., Henze, D. K., Ge, C., and Wang, W.: Inverse modeling of SO_2 and

838   NO_x emissions over China using multisensor satellite data – Part 2: Downscaling techniques for

839   air quality analysis and forecasts, Atmospheric Chemistry and Physics, 20, 6651-6670,

840   10.5194/acp-20-6651-2020, 2020b.

841   Wang, Y. X., McElroy, M. B., Jacob, D. J., and Yantosca, R. M.: A nested grid formulation for

842   chemical transport over Asia: Applications to CO, Journal of Geophysical Research: Atmospheres,

843   109, n/a-n/a, 10.1029/2004jd005237, 2004.

844 Zhang, L., Jacob, D. J., Knipping, E. M., Kumar, N., Munger, J. W., Carouge, C. C., van Donkelaar,
845 A., Wang, Y. X., and Chen, D.: Nitrogen deposition to the United States: distribution, sources, and
846 processes, Atmospheric Chemistry and Physics, 12, 4539-4554, 10.5194/acp-12-4539-2012, 2012.
847 Zhang, Q., Pan, Y., He, Y., Walters, W. W., Ni, Q., Liu, X., Xu, G., Shao, J., and Jiang, C.:
848 Substantial nitrogen oxides emission reduction from China due to COVID-19 and its impact on
849 surface ozone and aerosol pollution, Science of The Total Environment, 753,
850 10.1016/j.scitotenv.2020.142238, 2021.
851 Zhang, R. X., Zhang, Y. Z., Lin, H. P., Feng, X., Fu, T. M., and Wang, Y. H.: NOx Emission
852 Reduction and Recovery during COVID-19 in East China, Atmosphere, 11,
853 10.3390/atmos11040433, 2020.
854 Zhang, Y.-L. and Cao, F.: Fine particulate matter (PM2.5) in China at a city level, Scientific
855 Reports, 5, 14884, 10.1038/srep14884, 2015.
856 Zhao, Y., Zhang, K., Xu, X., Shen, H., Zhu, X., Zhang, Y., Hu, Y., and Shen, G.: Substantial
857 Changes in Nitrogen Dioxide and Ozone after Excluding Meteorological Impacts during the
858 COVID-19 Outbreak in Mainland China, Environmental Science & Technology Letters, 7, 402-
859 408, 10.1021/acs.estlett.0c00304, 2020.
860 Zheng, B., Tong, D., Li, M., Liu, F., Hong, C., Geng, G., Li, H., Li, X., Peng, L., Qi, J., Yan, L.,
861 Zhang, Y., Zhao, H., Zheng, Y., He, K., and Zhang, Q.: Trends in China's anthropogenic emissions
862 since 2010 as the consequence of clean air actions, Atmospheric Chemistry and Physics, 18,
863 14095-14111, 10.5194/acp-18-14095-2018, 2018.
864